Using the World Wide Lightning Location Network (WWLLN) to study Very Low Frequency transmission in the Earth-Ionosphere Waveguide: 2. Model test by patterns of detection/non-detection

Abram R. Jacobson[1] and Robert H. Holzworth

Earth and Space Sciences Dept., University of Washington, Seattle U. S.

and

James B. Brundell

Physics Dept., University of Otago, Dunedin NZ

1: Corresponding author Abram R. Jacobson, abramj@uw.edu

Abstract

This is the second half of a two-part study. In the first part, we had used the World Wide Lightning Location Network's recorded signal amplitudes to test a model of Very Low Frequency signal transmission from the lightning to each sensor. The model predicts a dramatic worsening of transmission at low magnetic latitudes, for nighttime propagation (compared to daytime propagation) toward magnetic West. However, we found that the use of amplitudes was ill-adapted for testing the model under conditions of a deep outage of transmission. Since the relative weakening of nighttime transmission is rather counter-intuitive, we have now developed an alternative approach to testing that model prediction. This alternative approach highlights the patterns of detection/non-detection of several low-magnetic-latitude WWLLN stations and compares those patterns with the appropriate patterns of the model transmission.

Key points

Suppression of low-latitude VLF transmission propagating magnetic West, especially in night.

New finding: The magnetic-westward suppression at night applies to nearly the entire westward half-plane, from magnetic-South clockwise to magnetic-North.

New finding: The magnetic-westward suppression at night is readily observable for dip angles in the range -30° to +30°.

Index terms: 2487, 6934, 6964,

1. Introduction

This is not a new topic. East-west asymmetry in VLF (Very Low Frequency; 3-30 kHz) propagation in the Earth-Ionosphere Waveguide had been inferred as early as the 1920's [see the historical review by *Crombie*, 1958]. The geomagnetic control over VLF propagation is expected to depend strongly on two orientational parameters [*Budden*, 1985; *Piggott et al.*, 1965; *Pitteway*, 1965; *Wait and Spies*, 1960; *Wait and Spies*, 1964; *Yabroff*, 1957]. One is the dip angle of the geomagnetic field, and the other is the propagation magnetic azimuth of the VLF wavefield. Along any long-range propagation Great Circle Path, both of these orientational parameters can widely vary. Thus, it is only very approximate to characterize the propagation magnetic azimuth "of the path" by its value at a path endpoint. The research results we review below can be broadly separated as to whether they just grossly consider the whole path together, or whether they dissect the path into small segments and use a different propagation azimuth and magnetic dip within each segment. The former we will call "bucket" approaches, in that they just characterize the entire path as being effectively at one propagation magnetic azimuth. By contrast, the model comparisons which consider the local nature of the two orientational parameters will be called "local" approaches.

All studies of the azimuthal asymmetry of VLF propagation prior to the present have been based on observing the effect of magnetic propagation azimuth on received amplitudes. This is equally true when the signals received were from narrow-band artificial beacons [e.g., *Bickel et al.*, 1970; *Pappert and Hitney*, 1988] or when derived from lightning strokes [e.g., *Hutchins et al.*, 2013; *Jacobson et al.*, 2021; *Taylor*, 1960]. In the already-published [*Jacobson et al.*, 2021] first

half of the present study, henceforth referred to as "JHB1", we followed the amplitude-comparison approach. However, we reached a cul-de-sac with that approach, when we tried to test a particular non-intuitive though impactful prediction of our model [*Jacobson et al.*, 2010; *Jacobson et al.*, 2009; *Jacobson et al.*, 2012]. The prediction is that for propagation at low dip angle, e.g. in the range -30 to +30°, propagation toward the magnetic West is deeply attenuated during dark-path conditions (night), *relative to sunlit-path (day) conditions*. Curiously, this counter-intuitive effect had not been overtly remarked prior to JHB1, though the physics package of the comprehensive, state-of-the-art path simulator, LWPC [*Pappert and Ferguson*, 1986], certainly contains all the relevant physics.

We found in JHB1 that the sought-after dark-path conditions apparently caused such a dearth of numerically sufficient lightning detections at the pertinent stations, so that amplitudes could not be determined with statistical accuracy. Thus JHB1 could not test its most interesting model prediction. "No detection, no amplitude".

This shortcoming of JHB1 motivated the present study, which is the second part of the study begun by JHB1. We completely change strategy in this paper. Rather than comparing amplitudes, we examine observed statistical patterns of detection/non-detection from ten selected stations. We compare those patterns to predictions of the model. The stations are chosen to represent all longitude sectors and all Universal Times, and to include many diverse paths from the lightning locations to the stations, in such a manner as to provide compelling statistical evidence on the model's predictions. The number of paths included exceeds 15-billion. Each of these paths is then dissected into 50 path segments, for a grand total exceeding 750-billion path

segments. At each path segment, the geomagnetic dip angle and magnetic propagation azimuth are calculated, along with the instantaneous solar zenith angle, are combined to predict the modeled contribution of that path segment to the overall integrated attenuation for that path.

2. Background

2a. Prior observations of east-west asymmetry of VLF propagation

Here we review the carefully documented work that began in the 1950's. Crombie described new measurements performed in New Zealand during 1957 [*Crombie*, 1958], one purpose of which was to investigate the asymmetry earlier hinted at by the scattered results of the 1920's. The 16.6-kHz signal from a powerful transmitter ("GBR") in Rugby, UK was received by a magnetic loop and a vertical aerial at Wellington, NZ. The receiver and the transmitter were nearly antipodal. By rotating the loop antenna, Crombie was able to select separately the signal arriving on either Great Circle Path, from respectively NNW or SSE (reckoned at Wellington.) The signal strength on each orientation of the loop was measured versus time during three multi-day periods. The results confirmed not only that the signal arriving from the NNW had 10-15 dB stronger amplitudes than the path arriving from the SSE, but also that the diurnal variations were dissimilar between the two paths. Crombie attributed this difference to the east-west components of each path, although this was left notional. The detailed variation of the magnetic azimuth along each path was not presented or addressed, so that Crombie's work was in the "bucket" category. The diurnal variation was not explained, but the gross difference between eastward and westward propagation was noted.

Shortly after the work by Crombie, there was a systematic attempt to use geolocated lightning to observe the zonal asymmetry of long-range broadband VLF propagation [*Taylor*, 1960]. Whereas Crombie had relied on a discrete, narrow-band, man-made beacon, Taylor exploited the powerful broadband emissions of lightning return strokes. Attention was focused on daytime conditions, with most of the paths over seawater. VLF receiver stations in the western United States and in Hawaii, triggering off common lightning strokes, were used to crudely geolocate the lightning, at least within <10% of the path length, by triangulating the direction found at each station. Each station measured and recorded the vertical electric field with a vertical mast, and also provided the direction of arrival from comparing signals on two vertical-magnetic-loop antennas. As was necessary in that era, data were recorded for off-line analysis using oscilloscopes and cameras. The east-to-west attenuation from twenty lightning discharges was used to determine a mean spectral attenuation (dB/1000km) for that direction of propagation. The spectral attenuation was determined for the entire VLF band. Similarly, the spectral attenuation for west-to-east attenuation was determined using sixteen lightning discharges. All observations were for entirely-daylit paths. It was found that attenuation east-to-west exceeded attenuation west-to-east, by approximately 3 dB/1000km for $f < 8$ kHz and by approximately 1 dB/1000km for $f > 10$ kHz.

Taylor's characterization of the paths as "east to west" versus "west to east" [*Taylor*, 1960] is in the bucket category. Moreover Taylor did not consider the control by geomagnetic dip angle; rather, all the paths were simply tagged as "east to west" or as "west to east", regardless of magnetic dip, and then simply labeled with one orientation. The lightning locations are not given

[*Taylor*, 1960], so it would not be possible to retrospectively model Taylor's observations with a more local approach.

In 1969, the United States Naval Ocean Systems Center conducted airborne measurements of VLF beacon signals on Great Circle Paths from the island of Hawaii toward San Diego and from the island of Hawaii toward Wake. The paths were, respectively, west-to-east and east-to-west paths, entirely over seawater, and entirely nighttime. These data were later presented and compared [*Pappert and Hitney*, 1988] to state-of-the-art, full-wave waveguide propagation calculations using the LWPC [*Pappert and Ferguson*, 1986]. The fixed frequencies of the beacons at Hawaii were discretely between 10.9 kHz (the lowest) and 28.0 kHz (the highest). The airborne receiver recorded signal amplitudes due to the multifrequency sounder for the first ~4000 km of each path. Thus the measurements were all done within 4000 km of Hawaii. The VLF data were compared to a model that included detailed tracking of the propagation azimuth and the magnetic dip angle locally at all points along the propagation path. This was a local approach, and was a critical advance over the bucket approach. It was found that the eastbound (San Diego path) signal was very reproducible day-to-day, and was essentially perfectly modeled by LWPC with a generic nighttime profile [*Pappert and Hitney*, 1988]. The westbound (Wake path) signal, by contrast, was more variable day-to-day, and this adversely affected the agreement with the model, although on average the agreement was satisfactory. The variability for westbound propagation was speculated to be related to sporadic electron-density features near altitude 90 km. We note that the sampled paths did not delve lower than about 30° in dip angle.

In addition to the airborne measurements using the multifrequency beacon, the same aircraft was also deployed to measure the signal from the unique 23.4-kHz signal "NPM" radiated from the area of Honolulu, Hawaii with much higher power than the research multifrequency beacon. The NPM signal was measured along Great Circle Paths from NPM toward Seattle, Ontario (California), Samoa, and Wake Island. Results were reported [*Bickel et al.*, 1970], similarly, out to ~4000 km range, and were entirely over seawater and at night. The authors [*Bickel et al.*, 1970] used an early predecessor of LWPC to compare with waveguide theory, and found that the model predictions of dependence on magnetic azimuth and magnetic dip angle were robustly confirmed at 23.4 kHz by the airborne measurements. Their model comparison was a local approach, exactly similar to that used for the multifrequency beacon data [*Pappert and Hitney*, 1988].

A more recent entry into the observation of propagation magnetic-azimuth asymmetry was done with the World Wide Lightning Location Network, or WWLLN [*Hutchins et al.*, 2013]. It dealt with over-seawater paths in the Pacific sector, using WWLLN stations at island locations Suva, Tahiti, and Honolulu. This study is in the "bucket" category. The study used lightning strokes jointly detected by all three of those stations (along with other stations as well.) Each lightning stroke's radiated VLF energy was determined with the WWLLN energy retrieval described elsewhere [*Hutchins et al.*, 2012]. The candidate strokes were selected according to the following strict limiting criteria:

(a) The WWLLN VLF energy determination for the stroke needed to have an estimated error less than 10% of the VLF energy.

(b) The stations participating in the location/energy determination needed to be equally distributed east/west of the stroke location, to within 25%.
(c) The strokes were limited to those for which the three paths to Suva, Tahiti, and Honolulu were *all* either less than 5% daylit *or* more than 95% daylit.

The strokes were selected from those occurring from May 2009 to May 2013. With these criteria, only 0.2% of the stroke population was accepted, that is, only $2X10^6$ strokes were accepted.

The high-confidence energy retrievals for the $2X10^6$ accepted strokes allowed each of these stroke's "normalized electric field" to be derived for each stroke, so as to use all the strokes despite their widely differing stroke VLF energies [*Hutchins et al.*, 2013]. The normalization was the rms measured electric field (in units of μVm^{-1}) divided by the square root of the retrieved VLF energy (in units of J). This normalization was tabulated for each of the strokes as the electric field in dB above 1 $\mu Vm^{-1}J^{-1/2}$.

The $2X10^6$ accepted strokes were grouped into azimuth/distance bins, with eight azimuth bins, each 45° wide, and distance bins 500 km wide. The azimuth was the average magnetic azimuth over the path, which is approximate, as the azimuth actually varies along each path. Within each bin, the bin median was used to show variations versus distance and azimuth. In order to highlight azimuthal variation, each attenuation rate was normalized by an "all-azimuth" average. Thus the normalized-attenuation data vary azimuthally with a mean of unity. The normalized-attenuation data were compared to the standard theory of idealized sharp-boundary reflection from a magnetized D-layer [*Wait and Spies*, 1960]. The agreement between the WWLLN results

and the sharp-boundary model was rather good [see Figure 5 in *Hutchins et al.*, 2013]. In part this agreement may be fortuitous. The model uses simply a sharp-boundary ionosphere, which is a problem. Moreover, the model did not explicitly treat "day" or "night", but rather tried two electron densities. However, the cited model stuck with $2X10^7$ s^{-1} as the fixed collision electron-neutral rate in the case of either of those electron densities, so they really do not illuminate the difference between night and day reflection conditions. Another cause for caution at the good agreement between the model and the data is that the model was for dip angle of 0°, whilst the range of dip-angle magnitude in the paths in the WWLLN study was 0° to ~45°. Therefore it is not ruled-out that the good agreement of the Wait model and the WWLLN data may have been partially fortuitous.

2b. Prior modeling of east-west asymmetry of VLF propagation

The reflection of radio waves from the underside of the ionosphere became an active area of research during the 1950s [see the historical references given by, e.g., *Barber and Crombie*, 1959; *Wait and Spies*, 1960; *Wait and Spies*, 1964; *Yabroff*, 1957]. The problem was nontrivial due to the anisotropy of the dielectric, associated with the gyration of charged particles about the geomagnetic field. This was especially true for VLF waves, whose height of reflection occurs in the lowermost ionosphere, namely the D-layer. The strong electron-neutral collision rate in the D-layer further complicates models of VLF reflection. The models needed to address practical challenges, e.g.:

(a) What is the VLF reflectivity?

(b) How does it depend on solar zenith angle?

(c) How does the reflectivity depend on angle-of-incidence?

(d) How does the reflectivity depend on local propagation magnetic azimuth (reckoned clockwise from local magnetic North) and on local magnetic declination ("dip angle")?
(e) How does the reflectivity depend on electron-neutral collision rate?

Starting late in the 1950's, sharp-boundary treatments of the collisional, anisotropic VLF reflection process were set up analytically and solved numerically with newly available digital computers [*Barber and Crombie*, 1959; *Wait and Spies*, 1960; *Wait and Spies*, 1964; *Yabroff*, 1957]. The first numerical model of an arbitrarily-layered (rather than just a sharp boundary) D-layer [*Piggott et al.*, 1965; *Pitteway*, 1965] followed quickly, although its physical implications appear to have been only slowly appreciated. The Pitteway model for the continuously varying D-layer solved the Maxwell Equations for the altitude-dependent, anisotropic, and complex susceptibility tensor. All of the sharp-boundary models, as well as the Pitteway model, dealt with the elementary reflection of an incident plane wave.

Such plane-wave models are excellent for providing insights on "process" questions, such as those cited in the previous paragraph. However, for long-range "multi-hop" propagation, it is more efficient, though less heuristically instructive, to cast the problem in terms of waveguide modes in the spherical-shell Earth-ionosphere waveguide (EIWG). The modes are akin to cylindrical waves from a point source within a parallel-plane waveguide, except that the waveguide elements are (approximately) *concentric spherical surfaces* [see the illuminating tutorial by *Cummer*, 2000]. A waveguide model provides a point-to-point complete description of the VLF transmission along any given Great Circle path. This includes all portions of the path. The first portion consists of 3-dimensional expansion of the wavefield into a hemisphere. The

next portion takes account of the first ionospheric reflection, which effectively is a transition to spherical-shell EIWG propagation. This transition needs many higher-order modes to describe the wavefield, because at such a short range (e.g, < 1000 km) a broad range of plane-wave "angles of incidence" are at play [*Cummer*, 2000]. Ultimately, however, at longer range the waveguide modes simplify. For a vertical-dipole source near ground level, and a vertical-dipole receiver also near ground level, the modes simplify at large distances to the fundamental Transverse Magnetic (TM) mode. Thus the transmission characteristics vary from 3-dimensional expansion into a hemisphere, to a single 2-D, fundamental TM mode in the waveguide.

The waveguide approach was perfected in the Long Range Propagation Capability, or LWPC [*Pappert and Ferguson*, 1986] suite of computer codes developed by the United States Navy. The LWPC includes an atlas of Earth-surface conductivity. The user can select a D-layer model, usually exponential profiles of electron density and of electron-neutral collision rate. The LWPC contains "everything" in one master code suite. LWPC uses just an approximation of the D-layer electron-density profile, but that is justified by the impossibility of knowing any better profile at any given instant.

One adverse side-effect of its end-to-end completeness is that the LWPC blurs (to the LWPC user) the role of *local* parameters, such as solar magnetic propagation azimuth and local magnetic dip angle. These vary along the path, but the LWPC's end-to-end approach path-integrates over their local variations, and all the user sees is the result of the path integration. Thus, despite its completeness, premiere accuracy, and reliability, the LWPC is not pedagogically illuminating for exploring individual local *processes* in isolation.

3. Recap of part 1 of the present study

3a. Plane-wave reflectivity and path transmission

This article is part 2 of a two-part study; here, we briefly recap the results of the first part, from JHB1. The work to follow entirely depends on JHB1, and the reader should refer to that published article for details beyond the brief recap here.

We rely on a numerical model of plane-wave reflection from a diffuse, collisional, anisotropic D-layer [*Jacobson et al.*, 2010; *Jacobson et al.*, 2009; *Jacobson et al.*, 2012]. Our model is a modernization of Pitteway's groundbreaking treatment [*Piggott et al.*, 1965; *Pitteway*, 1965]. We represent the electron-neutral collision rate by an exponentially declining function of altitude as is common in this field. For the electron density, we use an exponentially increasing function of altitude, also common in the field [see, e.g., Eq. 3.23, Section 3.2.3, in *Volland*, 1995]. See Table 1 for details.

Figure 1 summarizes the prediction of our plane-wave reflection model. The vertical axis is the amplitude reflection coefficient, R, from the D-layer for a typical long-range-propagation angle of incidence, in this case chosen as 85°. The reflection coefficient shown has been averaged over all frequencies from 5 to 20 kHz. As shown in JHB1, R varies continuously with solar zenith angle, but we show the pure-day and pure-night extreme cases only. On the left of Figure 1 is shown (a) the day-profile D-layer result, while on the right is shown (b) the night-profile D-layer

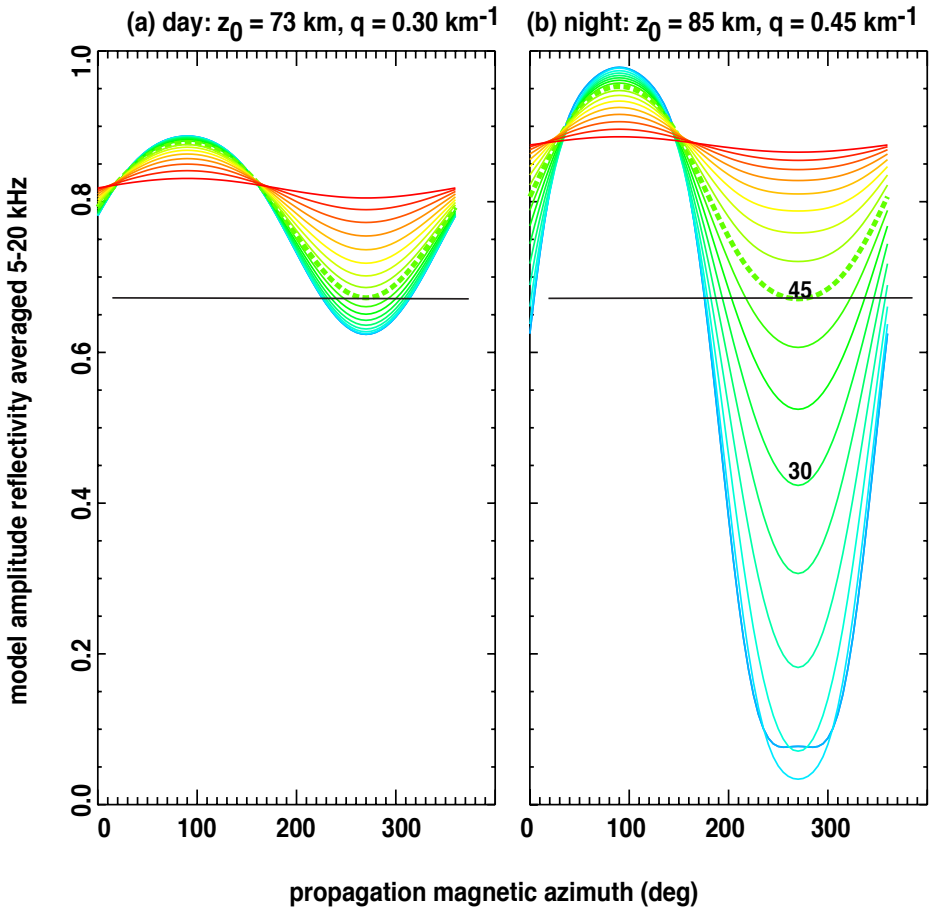

Figure 1: Model amplitude reflectivity (vertical axis) vs propagation magnetic azimuth (horizontal axis). Color marks magnetic dip angle, from 5° (blue) to 85° (red). Curve for dip angle = 45° is dashed. Model assumes angle-of-incidence is 85°, and is averaged over the band 5 - 20 kHz. (a) Day case. (b) Night case, with labels on curves for dip angle = 30, 45°. The horizontal black line on both panels is through the minimum of the curve for dip angle = 45.° in (b). See Table 1 for parameter values.

result (refer to Table 1 for profile parameters). The abscissa is the wave magnetic propagation azimuth. A separate curve is shown for each abs(dip angle), from 5° (blue) to 85° (red), in steps of 5°. The curves for dip = 30° and 45° are labeled in the night profile. For both (a) and (b), the curve for dip = 45° is dashed. The horizontal black line marks the nadir of the night-profile reflectivity level for dip = 45°.

How do we employ the single-reflection reflectivity from a plane-wave model, in the context of long-range ("multi-hop") propagation of quasi-cylindrical waves in a spherical-shell waveguide? The article on the first half of this project, JHB1, shows how this is done heuristically but with satisfactory agreement with observations: First, we correct the wave amplitude for the varying cross-sectional area of a ray-bundle on the spherical Earth (see Eq. 7 in JHB1). Second, we rely in JHB1 on a free parameter "r" , which is the effective number of reflections per reference distance ρ_0 = 1000 km (= 1 Mm). In JHB1 we demonstrated how comparison with observed received electric-field amplitude resulted in a fit for r in the range $3 > r > 2$.

Those two heuristics (correcting for the ray-bundle area, and invoking an effective reflection-per-pathlength) were used in JHB1 to crudely approximate long-range waveguide transmission in terms of the single-hop, plane-wave reflectivity model. We define a "logarithmic reference transmission", *assuming perfect ground conductivity*, along the Great Circle Path segment $L_{i,m}$ from VLF emission point "m" to sensor point "i" :

$$ln(ref.transmission) = \frac{1}{\rho_0}\int_0^{L_{i,m}} ln(R[Z_{i,m}(t_0), \alpha_{i,m}, I_{i,m}])ds_{i,m} + C(L_{i,m}) \quad \text{Eq. (1)}$$

where

$L_{i,m}$ = arcdistance along Great Circle Path from lightning location m to station i

$Z_{i,m}(t)$ = time-dependent, location-dependent solar zenith angle along path i,m

$\alpha_{i,m}$ = location-dependent magnetic propagation azimuth along path i,m

$I_{i,m}$ = location-dependent magnetic dip angle along path i,m

$R\,(Z_{i,m}(t), \alpha_{i,m}, I_{i,m})$ local instantaneous plane-wave reflectivity

$ds_{i,m}$ = differential path element along Great Circle Path i,m

ρ_0 = 1000 km

The term $C(L_{i,m})$ in Eq. (1) is the geometrical correction due to the variation of ray-bundle cross-sectional area. We tabulate the correction, relative to its value at the reference distance 1000 km:

$$C(L_{i,m}) = ln\left\{\sqrt{\frac{sin(\rho_0/R_E)}{sin(L_{i,m}/R_E)}}\right\} \qquad \text{Eq. (2)}$$

where R_E is the Earth's radius.

The logarithmic reference transmission (Eq. 1) must be multiplied by the fitted parameter *r* to give an estimate of the actual logarithmic path transmission *assuming zero ground losses* (see Eq. 9b in JHB1). This r parameter was fitted to lie in the range of 2 to 3. Physically, it is the number of hops per 1000 km reference distance, subject to our model's assumption of 85° angle-of-incidence.

Ignoring ground losses would be unacceptable if we were trying to calculate absolute transmission in the waveguide. However, our application involves examining the difference between day and night conditions on the propagation anisotropy. The ground conductivity effects

are unchanged (on a given path) between day and night. Thus modeling only D-layer losses is a satisfactory (though not perfect) approach for our study of day-versus-night differences.

A further convenient simplification introduced in JHB1 is that we actually solve for the log reflectivity ln(*R)* only for the two extreme cases of pure day and pure night. Any intermediate case is approximated by a linear combination of pure-day and pure-night, using a smooth function of solar zenith angle (see Eqs. 10-11 in JHB1). *This is done locally, at each point along the path integral in Eq. (1), and for local solar zenith angle obtaining at the instant of the lightning stroke.* There is a crucial difference between, on the one hand, making the linear combination locally (which we do), versus, on the other hand, evaluating the path integral along the entire path both for an artifactual day and an artifactual night case, then taking a linear combination of those two results based on the proportion of the path that is daylit. The latter approach would be clearly incorrect.

3b. Disfavoring of nighttime (relative to daytime) magnetic-westward propagation

Note that for abs(dip angle) < 45°, the night-profile reflectivity (Figure 1b) for propagation toward magnetic west (270°) is *less than the day-profile reflectivity (Figure 1a)*. This favoring of daytime over nighttime transmission for abs(dip angle) < 45° actually applies over a broad azimuth sector centered on magnetic west. Thus, for essentially half of all possible dip angles, and for essentially half of all possible propagation magnetic azimuths, the *nighttime reflection is predicted by our model* [*Jacobson et al.*, 2010; *Jacobson et al.*, 2009] *to be disfavored relative to the daytime reflection, and for small dip angle deeply disfavored*. This surprising and counter-intuitive feature is not remarked elsewhere in the VLF literature, and thus the burden is on us to

provide observational support for this counter-intuitive claim. Intuition would suggest that nighttime propagation should be *less* lossy than daytime, because the nighttime reference height (85 km in our model) has only 17% as much electron-neutral collision rate as does the daytime reference height (73 km in our model).

The remainder of this article relies on the first part of the study (JHB1) for a detailed development of the model theory. Readers should consult JHB1, which was published as Open Access and hence is without cost to the reader.

3c. Summary of observational results from part 1 of the present study

We presented in JHB1 a method to study the behavior of the inter-station ratio of VLF stroke amplitudes, for strokes that are simultaneously recorded at multiple WWLLN stations. This approach combined numerous recurrent strokes from long-duration lightning clusters to build a time-series of the ratio for a major portion of the UT day. The time variations of the sliding-averaged ratio are dominated by transient excursions coinciding temporally with those periods when the solar terminator is present along one or both of the paths. See, e.g., Figure 2 in JHB1. This strongly motivates a model incorporating significant control by the solar zenith angle.

Our plane-wave model predicts that magnetic-westward propagation has less waveguide transmission than does magnetic-eastward propagation. *Crucially, the anisotropy is extremely magnified for a night ionosphere.* This anisotropy is modulated by magnetic dip angle: The anisotropy is strongest at low dip angle, and weakest at large dip angle.

To account for solar-zenith-angle control on the waveguide transmission, our model takes a weighted combination of pure-day and pure-night solutions, *determined locally for every path element along the Great Circle Path from the lightning to the WWLLN station, and for the exact Universal Time of the stroke*.

The model solution based on the plane-wave-reflection theory successfully accounted for the gross features of the solar-terminator transients; see, e.g, Figures 7-10 in JHB1.

Our model predicts, counter-intuitively, that the magnetic-westward attenuation at low magnetic latitude will be much deeper during night than during day conditions. Unfortunately, this suppression of magnetic-westward propagation also largely eliminates the availability of sufficiently numerous recurrent recordings of those signals at our low-latitude stations. Thus the amplitude-ratio method pursued in JHB1 was inherently unable to check on the model's most intriguing and counter-intuitive prediction.

Thus our method to follow, rather than using lightning detections that exist, is designed to demonstrate the pattern of where and when detections do *not* exist.

4. WWLLN evidence on day/night differences in anisotropic VLF propagation

4a. WWLLN database

The overall epoch for this study is 1 December 2009 through 31 May 2021, Universal Time (UT). Within that overall epoch, numerous WWLLN recording stations began operation,

occasionally interrupted operation, and (in a few cases) ceased operation. For much of the overall epoch, at any time WWLLN had > 50 active stations worldwide. At present (2021) the census is > 60 active stations.

Our methodology in the following is to develop statistics on the *patterns of detection and non-detection by selected stations.* We use the entire WWLLN network product to define the overall population of WWLLN-located lightning strokes. This population is defined in a separate day file for each UT day. We then focus on ten selected stations located at magnetic low and mid latitudes. We develop statistical maps of the detection/non-detection of the overall WWLLN stroke population, by each of these ten selected stations.

To clarify "detection", we mean that a particular stroke is "detected" by a particular station *if that station participates in the solution for that particular stroke's location*. This is a stringent definition of "detection", compared to a more permissive definition that the station records a signal (whether or not that signal has the requisite amplitude and signal-to-noise to allow participation in the network solution.) The problem with the permissive definition is that one can never be sure, or even reasonably sure, that a signal is associated with a given stroke, if that signal cannot be used in the position/time solution for that stroke.

Table 2 lists pertinent metadata about the ten selected stations. Three of the stations (Atuona, Tahiti, and Honolulu) are in the Pacific ocean and have dominantly over-seawater paths from abundant lightning in both their Eastern and Western sectors. Another station (Costa Rica) is on

a relatively narrow land bridge between major oceans. Two stations (Peru and Dakar) are on the western periphery of lightning-rich continents.

For the statistics on each of the ten selected stations, we define a latitude band within which to include WWLLN strokes. This band is -40 to +40° N for nine of the stations, but for Honolulu the band is displaced to -30 to +50° N, in order to include the strokes in the northern continental United States. The population of WWLLN strokes within the latitude band is used to detect detection/non-detection by the respective selected station.

The population of WWLLN strokes within the latitude band and available for detection by the respective selected station varies from a maximum of $> 2X10^9$ strokes (for both Honolulu and Tel Aviv) down to $3.2X10^8$ strokes (for Belem). This disparity is driven mainly by the difference between the number of operating days for Honolulu (3873) or for Tel Aviv (3987), versus for Belem (566) within the overall epoch.

4b. Qualitative demonstration of geomagnetic and zenith-angle control over detection

Before embarking on a systematic quantitative analysis, we show a qualitatively clear example of the control over detection exerted by solar zenith angle and by geomagnetic parameters. Figure 2 shows the case of Atuona station, near the mid-Pacific. This example conveniently illustrates the situation for low dip angle and nearly-zonal magnetic propagation azimuth everywhere along the paths eastward and westward to regions of abundant lightning. In Figure 2, the station is a black rectangle symbol. In Figure 2(a), to the East of Atuona is shown a red rectangular box in northwestern South America. We select all WWLLN strokes within that box. For each stroke

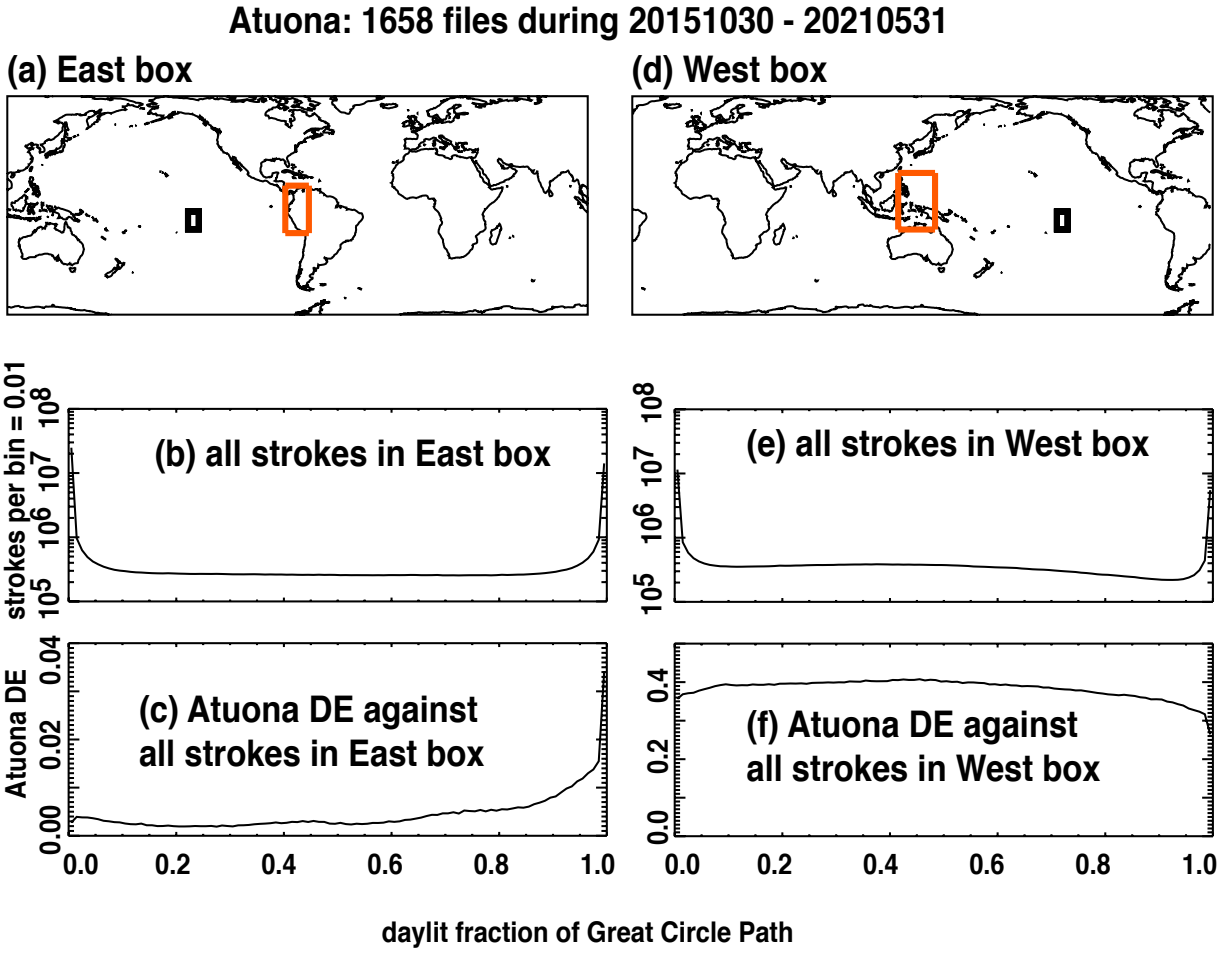

Figure 2: Comparison of observed Atuona detection efficiency against strokes in two roughly equidistant, rectangular geographic boxes. (a) Showing the East box, over northwestern South America. (b) For all strokes in East box, showing the distribution of fraction of instantaneous path (to Atuona) that is daylit. This includes all strokes in the East box, not just those detected by Atuona. Horizontal resolution is 0.01. (c) Detection efficiency (DE) of Atuona against strokes in East box, as a function of the instantaneous daylit fraction of the path. (d) Showing the West box. (e) For all strokes in West box, showing the distribution of fraction of instantaneous path (to Atuona) that is daylit. (f) Detection efficiency (DE) of Atuona against strokes in West box, as a function of the instantaneous daylit fraction of the path. Note the order-of-magnitude difference in DE scales between (c) East and (f) West boxes.

within that box, we calculate the solar zenith angle (at D-layer height) for all points along the path to Atuona from the stroke, and characterize each stroke by the proportion of the path that is in daylight. Figure 2(b) shows the daylit-fraction distribution of all strokes in the red box of Figure 2(a). The distribution is flat except for roughly equal peaks both at pure-dark (daylit fraction = 0) and at pure-daylit (daylit fraction = 1). We now ask, what is the Atuona detection efficiency (DE) for these strokes, versus the daylit fraction parameter? This is shown in Figure 2(c). The DE peaks toward maximum daylight, and is suppressed (by an order of magnitude) for daylit fraction < 0.6.

Now let us define a "control" case, which is shown in the right column of Figure 2. Figure 2(d) shows in red a "West box" over the Australasia sector. It is slightly further from Atuona than the East Box, but is roughly comparable in dip angle along the paths to Atuona. Figure 2(e) shows the daylit-fraction distribution for all strokes in the West box. Figure 2(f) shows the DE for Atuona detection of those strokes, as a function of daylit fraction. Now the DE for eastward propagation is relatively indifferent to daylit fraction, and the median DE for the west box is two orders-of-magnitude higher than the median DE for the East box (Figure 2c), and one order-of-magnitude greater than the maximum DE for the East box (Figure 2c). We note that this is a case where the paths to Atuona from either the West or the East box are everywhere quasi-zonal in magnetic azimuth, and are everywhere at very small dip angle (-20° to +20°). We chose this because of its convenience for a qualitative exercise like Figure 2.

This example qualitatively demonstrates, within the context of low dip angle, (a) the dramatic difference between propagation at eastward magnetic azimuth versus westward magnetic

azimuth, and (b) the extreme favoring of daylit propagation over night propagation for westward magnetic azimuth. This latter feature has not previously been remarked in the VLF literature.

4c. Geomagnetic context for the ten selected stations

We now show the geomagnetic context of each of the ten selected stations and of the propagation paths connecting them to lighting strokes in their respective latitude band described in Table 2. The geomagnetic model is the International Reference Geomagnetic Field, or IGRF [*V-MOD*, 2010]. Figure 3 contains a separate panel for each of the ten stations. Color indicates the geomagnetic dip angle's absolute value, in°. Black is dip = 0°. For nine of the panels, red is 74°, while for one (Figure 3i, Honolulu) the band is offset and the maximum dip angle is 76°. In addition to color-coding, discrete curves of |dip| = 30, 45° are overlaid on the map. The station is marked with a rectangle symbol, either white or black, to contrast with its immediate background color. The color shading covers the latitude band in which strokes are considered for detection/non-detection by the respective station.

Because of the extremely low transmission of VLF over Antarctic (or, to a lesser extent, Arctic) ice, we wish to exclude strokes whose Great Circle paths to the selected station reach further poleward than geographic latitude +/- 55°. This excludes strokes roughly within a cone centered on the respective station's antipode, which we blank-out with white. Thus, for example, in Figure 3(a) the antipode of Atuona is situated near the southern Red Sea. Each station has its own antipode, and cone centered there, in which we do not gather statistics regarding stroke detection by that station.

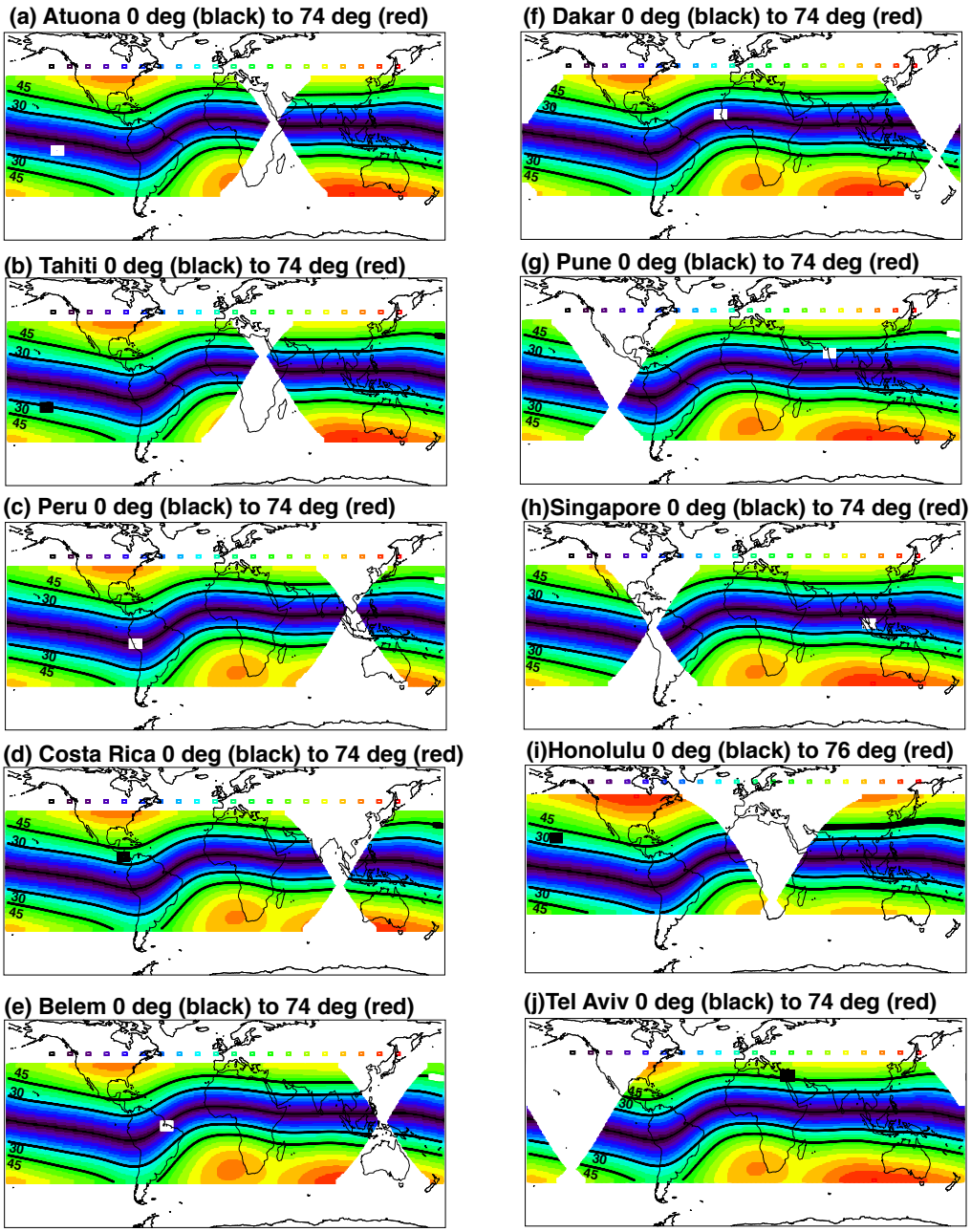

Figure 3: Geomagnetic setting of each of the ten selected stations. Each station is shown as a rectangle, either white or black so as to contrast with the background. The color shading of the background is magnitude of dip angle, from 0 (black) to 74° (red). Only (i) has a different color scale: 0 (black) to 76° (red). The colors are shown within latitude bands -40 to +40°, except -30 to +50° for (i) Honolulu. Also, discrete curves are drawn, where dip angle = -30, -45, +30, and +45°. The white cone at each station's antipode is excluded from the analyses, because the Great Circle Paths from strokes within those cones extend poleward of +/- 55° latitude.

Recall that the model results (Figure 1) predict a nighttime increase of attenuation for propagation toward magnetic West, relative to daytime, for |dip angle| < 45°. This nighttime increase in attenuation toward magnetic West becomes especially severe for |dip angle| < 30°. Figure 3 shows visually that this band of enhanced nighttime westward attenuation occupies most of the important lightning prone areas [*Christian et al.*, 2003], excepting only the continental United States. That is, the nighttime disfavoring of magnetic-westward VLF propagation is not going to be a mere academic curiosity confined to a small region, but rather applies to most regions of relevance to global VLF lightning location.

4d. Spatial patterns of observed and predicted detectability

4d.1 Approach

We now start a formal comparison of the observed and predicted detection patterns of each of the ten selected stations. Separately for each station, we define two cohorts of strokes within the accepted latitude band. The day cohort contains the strokes whose Great Circle Paths to the station are > 80% sunlit at the instant of the stroke, at D-layer height. This day cohort represents mostly-daytime propagation. The day cohort contains the strokes whose Great Circle Paths to the station are < 20% sunlit, representing mostly-nighttime propagation.

In addition to those statistics based on observation, we calculate the logarithmic reference transmission (Eq. 1 above) for each Great Circle Path under two artificial conditions: that the entire path be either in daylight or in darkness. These yield "day" and "night" logarithmic reference transmissions.

Finally, we calculate the instantaneous logarithmic reference transmission, *using the actual instantaneous solar zenith angle at each point along each path*, for all strokes. The distribution of logarithmic reference transmission shows the strokes that are *available* for the selected station to detect. The sub-distribution of logarithmic reference transmission *only for the strokes that are detected by the selected station* shows the relationship between detectability (by the selected station) and logarithmic reference transmission (relative to the selected station). We would expect that if the model has some correlation to observational reality, then the strokes detected by the selected station would be bunched at the high-transmission end of the distribution, and would be sparse or absent in the low-transmission end of the distribution. On the other hand, if the model were basically worthless, then there would be no strong correlation between observed detectability and model-predicted logarithmic reference transmission.

The reader should keep in mind that stations do not all have the same effectiveness in detecting lightning [*Hutchins*, 2014]. We will call this "sensitivity", but this does not mean something so simple as system gain. Rather, the two most important factors are, first, the level of background VLF noise affecting the selected station, and, second, the abundance of nearby lightning [*Hutchins*, 2014]. The effect of abundant nearby lightning is to reduce the ability of the station to participate in network detections of distant lightning strokes. This is because each WWLLN station has a software-adjusted trigger threshold for capturing a pulse to become a candidate for participation in a network location of strokes. The threshold is sluggishly (~2 minutes of inertia) adjusted, so as to continuously keep the rate of station triggers not greater than 3 per second. Abundant nearby lightning interacts with this feedback to increase the trigger level and thus reduce the ability of that station to trigger on distant lightning.

4.d2 Four case studies of patterns of detection/non-detection

Atuona case

Figure 4(a) maps the density of the day cohort of strokes, having mostly-sunlit paths to Atuona. The color scale is *relative to the maximum-density pixel in this plot*, with blue meaning 0.01 x maximum, and red meaning maximum. The resolution is 1° X 1°. The white areas are < 0.01 x maximum. The stroke density is displayed only within the -40 to +40° N band. The curves of |dip angle| = 30, 45° are shown in heavy black, while the geomagnetic equator is shown as a thinner black curve. Neither the |dip angle| curves, nor the stroke density, are shown within the antipodal cone. Also, the -45° dip-angle curve is not shown where (southmost South America) it is outside the latitude band.

Figure 4(b) is like Figure 4(a), *except that the density is only for the subset of the day-cohort strokes that are detected by Atuona*. Thus comparison of Figure 4(a, b) gives a visual map of the pattern of day-cohort detection/non-detection by Atuona. Note that the eastern two-thirds of South America's day-cohort lightning is not detected by Atuona, whilst the lightning in SE Asia and Indonesia, though no closer, is largely detected.

Reminder: The color range in the second panel, Figure 4(b), is determined *only* by the densities in Figure 4(b), and is *unrelated* to the color range in the first panel, Figure 4(a). Thus for example, the threshold for blue (0.01 x maximum) is different (and smaller) in Figure 4(b) than

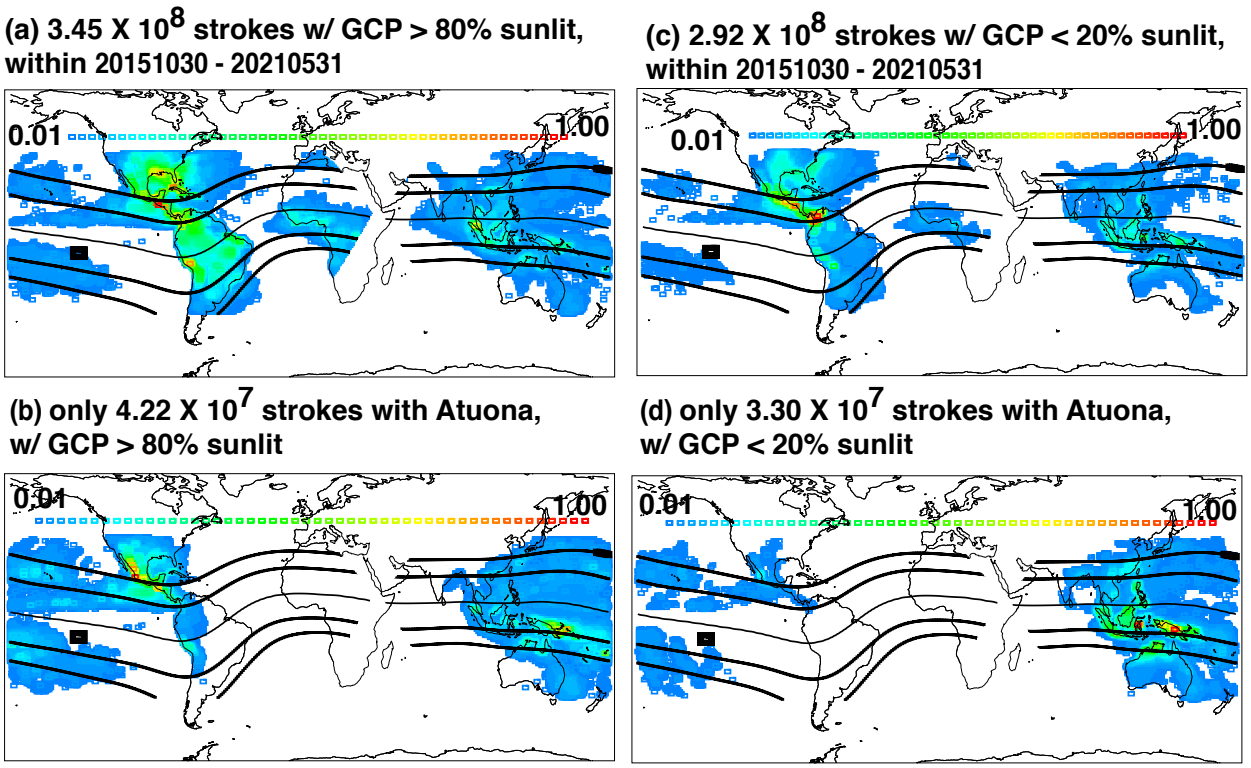

Figure 4: Patterns of detection/non-detection for Atuona. (a) Spatial density of WWLLN-located strokes within the latitude band for which the Great Circle Path is > 80% sunlit. The maximum for this density is red, while blue is 1% of the maximum. White areas outside of the antipodal cone correspond to stroke density less than 1% of the maximum. The discrete lines are at dip angle = 0, +/- 30, and +/- 45°. Neither the stroke density, nor the curves, are shown within the antipodal cone or outside of the latitude band. (b) Spatial density of the subset of strokes in whose location Atuona participates, for which the Great Circle Path is > 80% sunlit. The new maximum is shown as red, and 1% of this new maximum is shown as blue. (c) Similar to (a) but for Great Circle Paths < 20% sunlit. (d) Similar to (b) but for Great Circle Paths < 20% sunlit.

in Figure 4(a). This allows blue cells to appear in the second panel, in principle, at a few locations that are white (sub-blue) in the first panel.

Figures (4c-d) are exactly like Figures 4(a-b) except for the night cohort of strokes, having mostly dark paths to Atuona. In night conditions, the asymmetry becomes more dramatic. Atuona detections in South America become insignificant, whilst detection on the West robustly covers the Maritime Continent and all of Australia.

A problem with presenting the data as in Figure 4 is that the reader is forced to compare two panels (e.g., 4a to 4b; or 4c to 4d) in order to infer the spatial pattern of *detection efficiency*, which is after all what we are interested in. In order to make the detection efficiency more readily visualized, we show it directly in Figure 5. Figure 5(a) shows the ratio of the pixel values in Figure 4(b) above, to the pixel values in Figure 4(a) above, for the daytime cohort of strokes. The color scale goes from 0.00 (blue) to 0.82 (red). Because of the reduced statistics within any given 1° X 1° pixel, the result is somewhat noisy, but nonetheless suffices to show the gross geographic dependence of the observed Atuona detection efficiency. The white areas are either within the antipodal cone, or lack the minimum number of candidate strokes (1% of the global maximum) to be considered. This accounts for the patchy geographic coverage.

The model prediction of logarithmic reference transmission for the daytime model is shown in Figure 5(b), for all grid points within the selected latitude band, regardless of the incidence of lightning there. The only exception is that the transmission is whited-out in the antipodal cone. The displayed value is lumped into just four ranges of logarithmic reference transmission: > -2

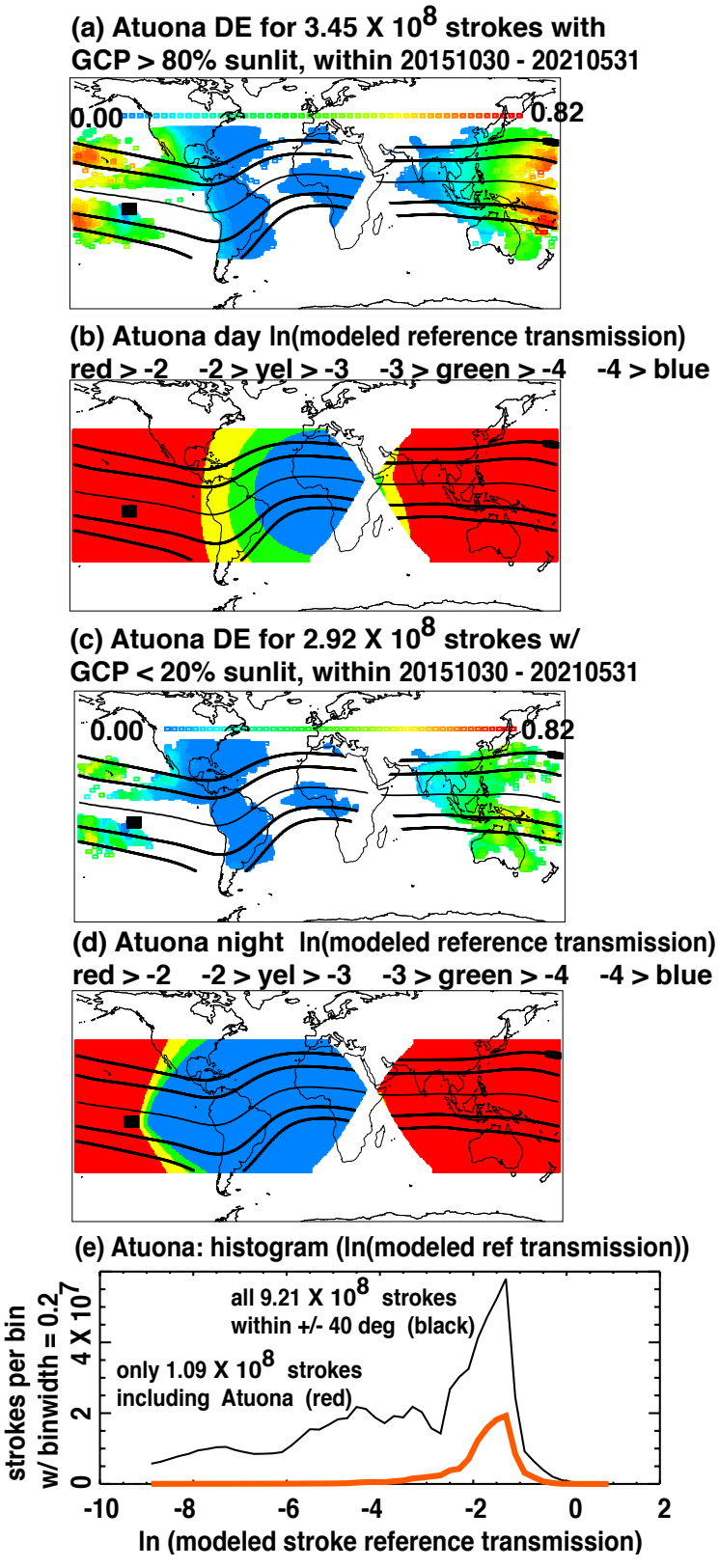

Figure 5: Observed and predicted results on Atuona detection efficiency. (a) Map of observed detection efficiency by the Atuona station for the strokes each of whose paths to Atuona are >80% sunlit. Color scale runs from 0.00 (blue) to 0.82 (red). Pixel resolution is 1° X 1°. White areas outside of the antipodal cone correspond to stroke density less than 1% of the maximum. The discrete lines are at dip angle = 0, +/- 30, and +/- 45°. (b) Predicted logarithmic reference transmission for the contrived pure-day case. The pixels are whitened in the antipodal cone and outside of the latitude band. The transmission values are shown as ranges from the highest transmission, > -2 (red), through less high, -2 to -3 (yellow), to even lower, -3 to -4 (green), to lowest transmission, < -4 (blue). (c) Similar to (a), but for the paths <20% sunlit. The color scale is the same as used in (a). (d) Similar to (b), but for the contrived pure-night case. (e) Distribution of the modeled logarithmic reference transmission, using exact instantaneous local solar zenith angle at each segment of each path from the stroke to the Atuona station. Black curve: All strokes within the latitude band. Red curve: Only those strokes in whose location Atuona participates.

(red), -2 to -3 (yellow), -3 to -4 (green), and < -4 (blue). The color red is used for high transmission, and the color blue is used for low transmission. In this way the predictions (Figure 5b) are placed on a color scale that is qualitatively similar to the color scale for the observed detection efficiency (Figure 5a): red is high and blue is low detection. Comparing the model prediction of logarithmic reference transmission (Figure 5b) with the observed detection efficiency shows that the two distributions are grossly consistent. *All* of the pixels with nonzero detection efficiency in Figure 5(a) occur either where the predicted logarithmic reference transmission greater than -3 (yellow band) and or where it is greater than -3 (red band). *None* of the pixels with nonzero detection efficiency in Figure 5(a) occur where the predicted logarithmic transmission is less than -3 (green and blue bands.)

Figures 5(c,d) are similar to Figures 5(a,b) except that they are for the nighttime cohort of strokes and for the nighttime model. The east-west asymmetry, which had already been noticeable for daytime (Figures 5a,b), is now more dramatic in nighttime conditions. During nighttime, Figure 5(c) shows that Atuona detection extends into India, but is zero over South America and very low over Central America. This is qualitatively consistent with the predicted pattern of transmission (Figure 5d).

Figure 5(e) shows histograms of the actual *instantaneous* logarithmic reference transmission, taking account of the *instantaneous solar zenith angle at each point along the path*. This is not the contrived "day" or "night" prediction of Figures 5(b,d). The black curve in Figure 5(e) is for all $9.21X10^8$ strokes within the latitude band, while the red curve is for only the $1.09X10^8$ strokes in that band detected by Atuona. By comparing the two curves, it is apparent that

Atuona's detection rate falls off rapidly for logarithmic reference transmission < -2, and is completely insignificant for < -4. These are empirical facts based on the distribution of lightning amplitudes, the proximity of the lightning to Atuona, the performance of the network, and the performance of this particular station. The empirical evidence of Figure 5(e) allows us to interpret the model predictions for contrived pure-day (Figure 5b) and contrived pure-night (Figure 5d). The red-shaded regions correspond to logarithmic reference transmission > -2. We can thus interpret the red regions in Figures 5(b,d) as having unimpeded detectability (at least as far as D-layer effects are concerned.) The yellow-shaded regions are predicted to have relatively lower detection success, though not zero. Green is even lower, and there are predicted to be essentially no detections in the blue-shaded regions, where logarithmic reference transmission is < -4. With that as a guide, we can now appreciate that the behavior of Figure 5(a) is roughly consistent with the contrived day model (Figure 5b) and the empirical distribution (Figure 5e). Similarly, the behavior of Figure 5(c) is roughly consistent with the contrived night model (Figure 5d) and the empirical distribution (Figure 5e). Notably, Atuona's complete non-detection of any lightning in South America for mostly-dark paths (Figure 5c) is consistent with the all-blue shading of South America (Figure 5d) in the night model. Likewise, Atuona's strong detection in the Australasia sector for mostly-dark paths (Figure 5c) is consistent with that region's being shaded red (Figure 5d) in the night model.

The map-based displays (Figures 5a-d) are useful for illustrating the geographic patterns of detection/non-detection by Atuona for two extreme cases, as well as comparing those patterns with the respective model predictions. However, these map-based displays are extremely

complicated to follow, and are patchy in their coverage due to the uneven geographical and temporal occurrence of lightning [*Christian et al.*, 2003].

Ultimately, the entire quantitative outcome of our data for Atuona can be distilled into the far simpler and clearer Figure 5(e), which uses *all* the available strokes in the latitude band, without parsing for contrived special cases (mostly-day, mostly-dark). The parent distribution (black curve) shows that > 50% of the network-detected strokes have logarithmic reference transmission (to Atuona) < -3, whilst by contrast, for the subset detected by Atuona (red curve) there are very few detected strokes in that range. Thus the predictive model is consistent with the pattern of Atuona's detection/non-detection. (We take as axiomatic that large signals tend to be easier to detect than are small signals.)

Peru case

Figure 6 shows the Peru case. The format is exactly the same as for Figure 5 above. The Peru station is situated on the west margin of a lightning-rich continent. Peru can detect almost only for predicted logarithmic reference transmission (to Peru) > -2.5 (Figure 6e). In the daytime case (Figure 6a), Peru can detect well throughout South America. In the nighttime case (Figure 6c), Peru cannot detect strokes in the eastern half of its own continent, even as it detects in far more distant Micronesia. This is well predicted by the model in Figures 6(b,d). All the quantitative outcomes of the data for Peru are summarized in Figure 6(e)), and it indicates the model is consistent with the Peru station's detection/non-detection. If the model were fundamentally

inconsistent with the observations, then the red curve in Figure 6(g) would not be so selective for the high-transmission end of the abscissa.

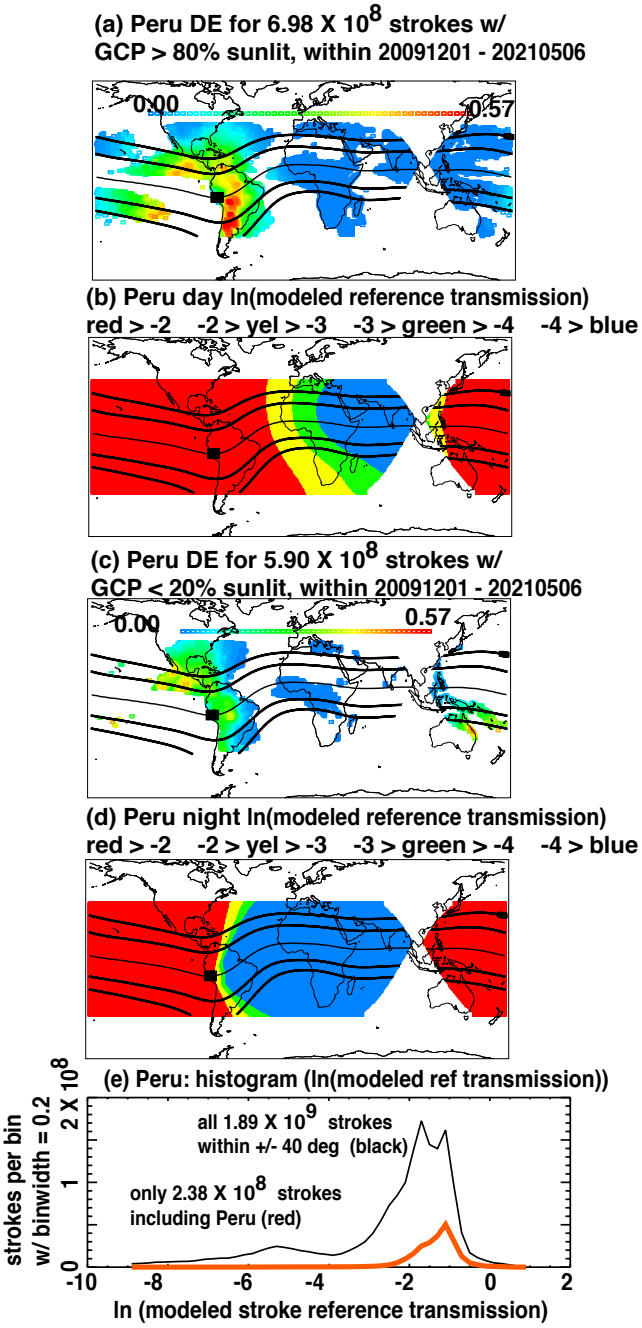

Figure 6: Similar to Figure 5, but for Peru station.

Singapore case

Figure 7 shows the Singapore case, in the same format as Figures 5-6 above. Singapore detections are mostly confined to strokes whose predicted logarithmic reference transmission (to Singapore) > -2.3 (Figure 7e). The geographical patterns for the night cohort of strokes show extreme asymmetry favoring strokes on the West of the station and disfavoring strokes on the East of the station. The pattern of detection/non-detection by Singapore is grossly consistent with the model predictions (Figures 7 b,d).

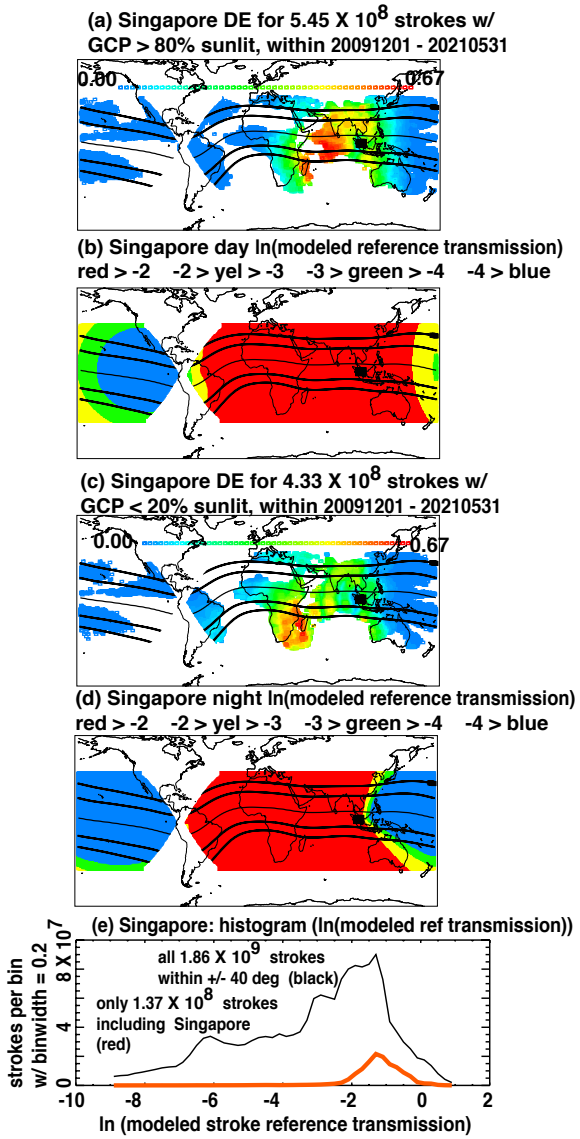

Figure 7: Similar to Figure 5, but for Singapore station.

Honolulu case

We complete this part of the survey with a selected station situated at higher magnetic latitude compared to Atuona, Peru, and Singapore . Figure 8 shows the Honolulu case. The bulk of Honolulu's detections are for strokes whose predicted logarithmic reference transmission (to Honolulu) > -2.5 (Figure 8e) with a low tail out to -4, as had been the case with Atuona. For the nighttime cohort of strokes (Figures 8c), Honolulu detects very few strokes in South America, whilst its more distant detections on the West go all the way across India. The Honolulu patterns of detection/non-detection are grossly consistent with the model predictions (Figures 8b,d,e). Significantly, Honolulu maintains significant nighttime detection (Figure 8c) to the East, over the continental United States, consistent with the higher dip angle along the Honolulu-to-lightning paths there. Recall that the model predicts (Figure 2 above) that for dip magnitude > 45°, there is no disfavoring of westward relative to eastward transmission.

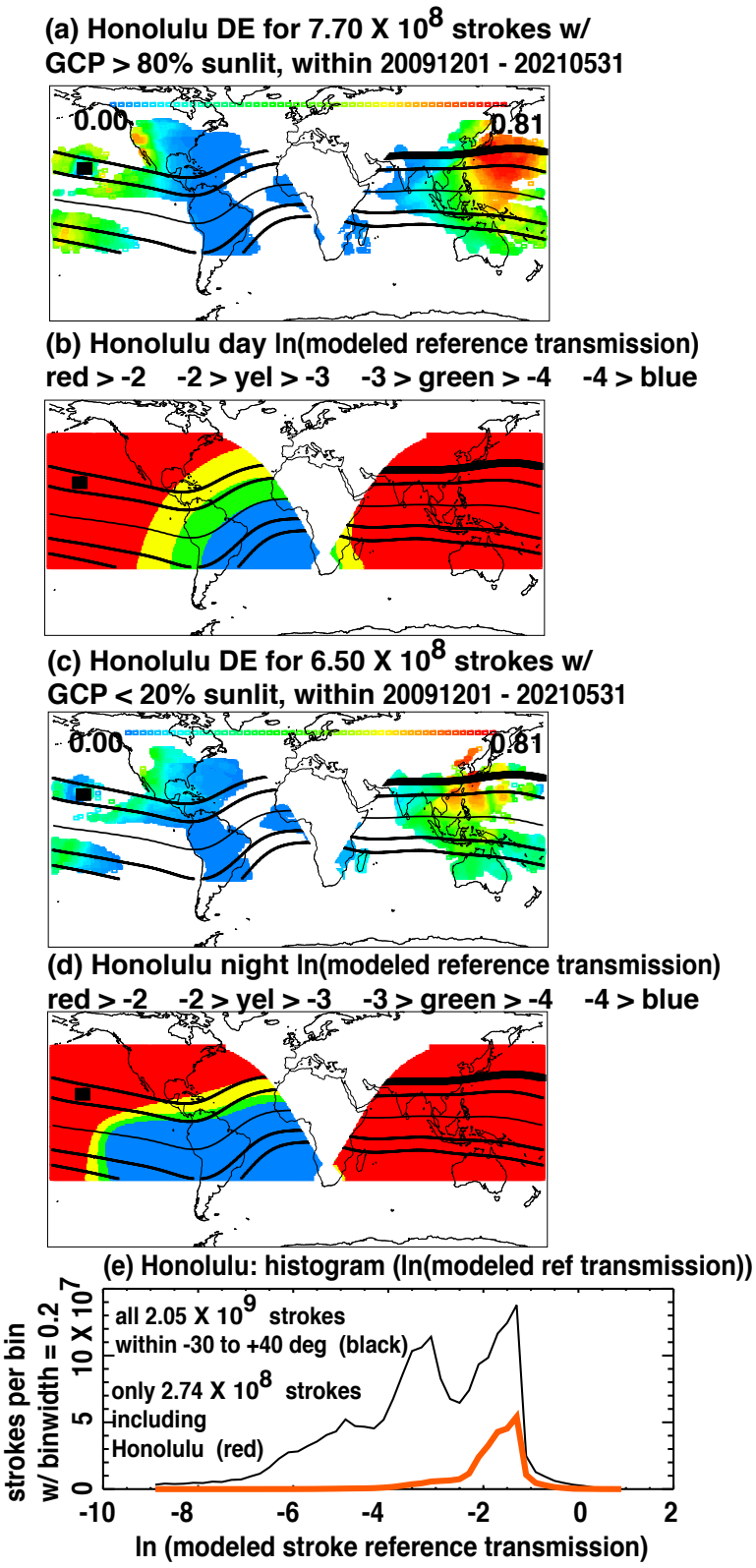

Figure 8: Similar to Figure 5, but for Honolulu station.

The remaining six of our ten stations' detection-efficiency results will presented in the Appendix.

5. Conclusions

This is the second part of a two-part study of broadband VLF propagation from lighting strokes to WWLLN stations. The first part of the study (JHB1) had developed a model for the effects of the ionospheric D-layer on long-range VLF transmission in the Earth-Ionosphere Waveguide. The model makes the counter-intuitive prediction that, for dip angles in the range -30 to +30°, propagation toward the west half of magnetic azimuths will be dramatically worse during conditions of darkness (along the propagation path) than during conditions of daylight. This feature had never been remarked before in the literature, although it is in fact also embedded in the standard LWPC code. We surmise that the reason the feature had never been remarked is that the LWPC is an end-to-end treatment that tends to obscure, to the code's user, the details of differential transmission at any one point on the propagation path.

Our model had been applied in JHB1 to explaining the inter-station ratios of signal amplitudes from the same stroke at different stations. That approach, in common with all virtually all other approaches done by prior workers, was based on the measurement of VLF amplitudes. However, we found that the amplitude-based method was inadequate to the test the model's counter-intuitive prediction regarding the day/night control of westerly propagation. That is because the

amplitude-based approaches require detections in order for amplitudes to be determined. "No detections, no amplitudes".

This second part of the study circumvents that problem by adopting an opposite approach. Rather than use received signal amplitudes as the raw data, we now use the observed statistical patterns of detection/non-detection. We compare those patterns to our model's predictions of the D-layer contributions to path transmission. By focusing on the variations between daylit and dark conditions, we also avoid the confounding effect of ground losses, as the latter are invariant between daylit and dark conditions.

We highlight the geographical patterns of detection/non-detection from each of ten selected stations arranged around diverse longitudes. For each of these stations, we identify strokes whose paths are either mostly daylit or mostly dark. The patterns of detection/non-detection in these two special cases are then compared with the predictions of our transmission model, for either all-lit paths or all-dark paths respectively. The spatial agreement between observation and model is good. We then use *all* the strokes, not just those whose paths are mostly lit or mostly dark, and calculate the modeled logarithmic reference transmission along each stroke's path to the selected station, taking account of the instantaneous solar zenith angle at each point along the path. We tally the distribution of logarithmic reference transmission, both for the parent population of strokes, and for the subset of strokes that are detected by the selected station. We find consistently, for all of our selected stations, that the detected subset's distribution of logarithmic reference transmission is entirely crowded to the high-transmission end. This suggests that the model's predictions of transmission are pertinent.

Finally, and most importantly, our ten case studies robustly demonstrate that for dip angles in the range -30 to +30°, during conditions of darkness there is dramatically worse transmission from magnetic East to West then from magnetic West to East, whereas for daylit conditions, this is much less pronounced. These findings are operationally significant for long-range lightning detection. For example, WWLLN's Pacific stations Atuona, Tahiti, and Honolulu are not able in dark-path conditions to contribute significantly to locating lightning in South America, though they are extremely useful over comparable distances with lightning in Australasia. Similarly, under dark-path conditions, Peru basically misses the eastern half of its own continent, and Dakar sees even less of its own continent. For the same reason, during dark-path conditions, Pune is very good for detecting lightning in Africa but misses almost all lightning at similar distances in Australasia. These effects are not subtle, when viewed geographically in terms of areas of detection and non-detection.

Appendix

Tahiti case

Tahiti is close to Atuona though at somewhat larger |dip angle| ~ 30°. Figure A1 is like Figure 5, but for the Tahiti case. Because Tahiti has operated during almost the entirety of the study epoch, it has more strokes in the parent distribution ($1.94X10^9$). The Tahiti detections are almost entirely confined to logarithmic reference transmission (to Tahiti) > -2.5 (Figure A1e), consistent with being a less sensitive station than Atuona. Tahiti almost totally fails to detect lightning in

the Americas in night conditions (Figure A1c), while Tahiti is highly successful with the Australasia sector.

Again, as commented earlier in the case of Atuona (Figure 5), all the quantitative evidence from Tahiti data is condensed into Figure A1(e); the geographical map presentations of detection efficiency are qualitative by comparison. And again, the sharp cut-off of the red curve in Figure A1(e) shows that the model has predictive value for Tahiti detection/non-detection.

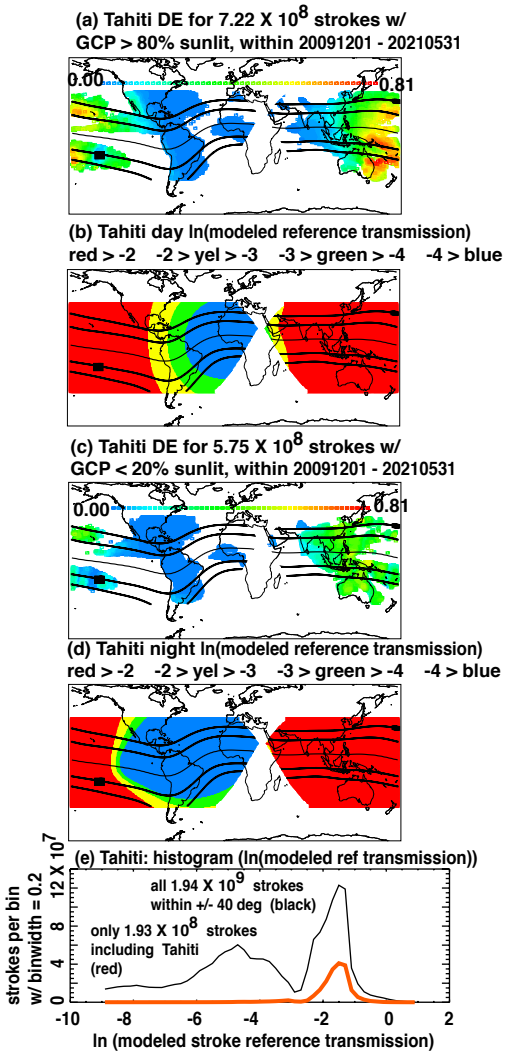

Figure A1: Similar to Figure 5, but for Tahiti station.

Costa Rica case

Figure A2 shows the Costa Rica case, in the identical format as Figure 5. Costa Rica can detect mostly for predicted logarithmic reference transmission (to Costa Rica) > -2.5 (Figure A2e). During night conditions (Figure A2c), Costa Rica loses detection for strokes in much of eastern South America. During those same night conditions, Costa Rica gains detections in the far more distant Australasia and Micronesia sector, where there are few daytime detections (Figure A2a). All the quantitative outcomes of the data for Costa Rica are summarized in Figure A2e, and it indicates the model is consistent with the Peru station's detection/non-detection.

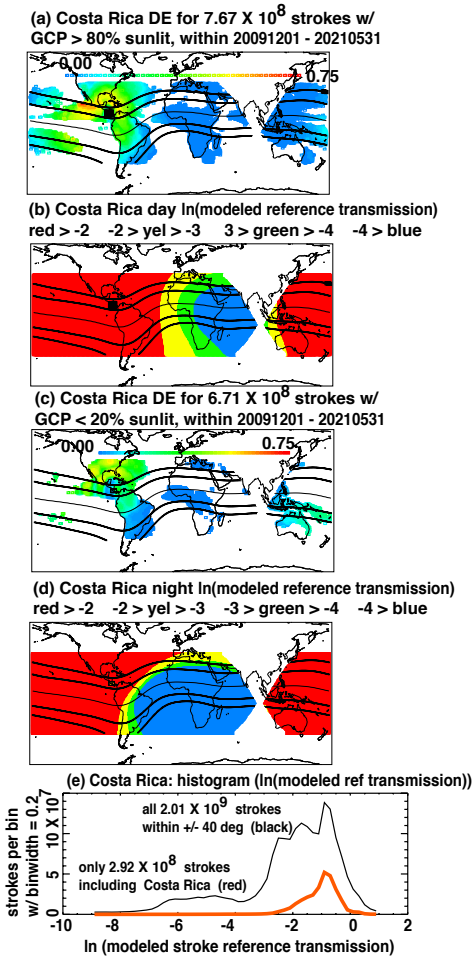

Figure A2: Similar to Figure 5, but for Costa Rica station.

Belem case

Figure A3 shows the Belem case, in the identical format as Figure 5. One of our least sensitive stations, Belem is essentially unable to detect for strokes whose predicted logarithmic reference transmission (to Belem) < -2.0 (Figure A3e). Some of western Africa lightning is detected by day, but nothing by night. This is consistent with the day and night model predictions (Figure A3b,d). All the quantitative outcomes of the data for Belem are summarized in Figure A3(e), and it indicates the model is consistent with the Belem station's detection/non-detection.

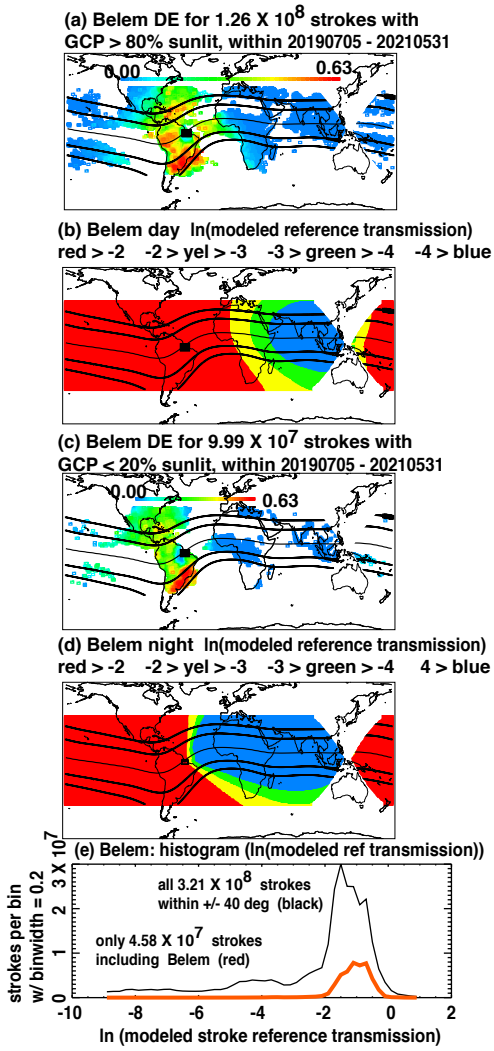

Figure A3: Similar to Figure 5, but for Belem station.

Dakar case

Figure A4 shows the Dakar case, in the identical format as Figure 5. Like Peru, Dakar lies on the western edge of a lightning-prone continent. Figure A4(e) shows that Dakar cannot detect lightning whose predicted logarithmic reference transmission (to Dakar) < -2.0. During daytime Dakar can detect strokes in all but the easternmost part of Africa (Figure A4a), but during the night (Figure A4c), Dakar loses all of Africa coverage save for the western bulge proximal to the station itself. All of these Dakar effects are grossly consistent with the model predictions in Figures A4(b,d).

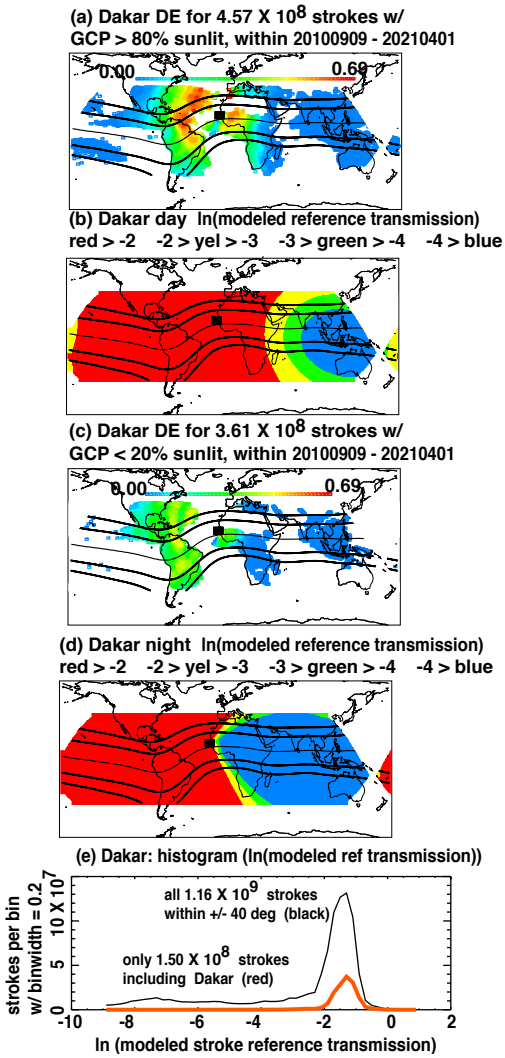

Figure A4: Similar to Figure 5, but for Dakar station.

Pune case

Figure A5 shows the Pune case, in the identical format as Figure 5. Pune is between Australasia's and Africa's lightning-prone regions. As seen in Figure A5(e), Pune's detections are almost all for strokes whose predicted logarithmic reference transmission (to Pune) > -2.3. During nighttime (Figure A5c) but not during daytime (Figure A5a), Pune can detect significant lightning in eastern South America. Similarly, during nighttime (Figure A5c) Pune cannot detect lightning further east than Thailand, while in daytime (Figure A5a), Pune's detection extends further eastward over Borneo. These are predicted by the model in Figures A5b,d). The model predictions are consistent with the pattern of Pune detections/non-detections.

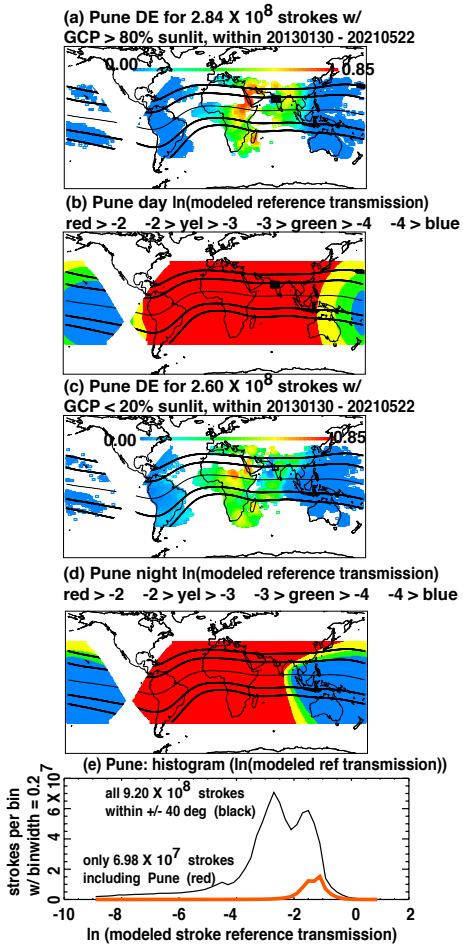

Figure A5: Similar to Figure 5, but for Pune station.

Figure A6 shows the Tel Aviv case (with identical format as Figure 5), located at dip angle > 45°. Virtually all of Tel Aviv's detections are for strokes whose predicted logarithmic reference transmission (to Tel Aviv) are > -2.5 (Figure A6e). Despite its relatively high magnetic latitude, long range detection eastward or westward into the low magnetic latitudes still displays the asymmetry favoring strokes from South America over strokes in Australasia, particularly for the night cohort (Figure A6c). The Tel Aviv pattern of detection/non-detection is grossly consistent with the model predictions (Figures A6b,d).

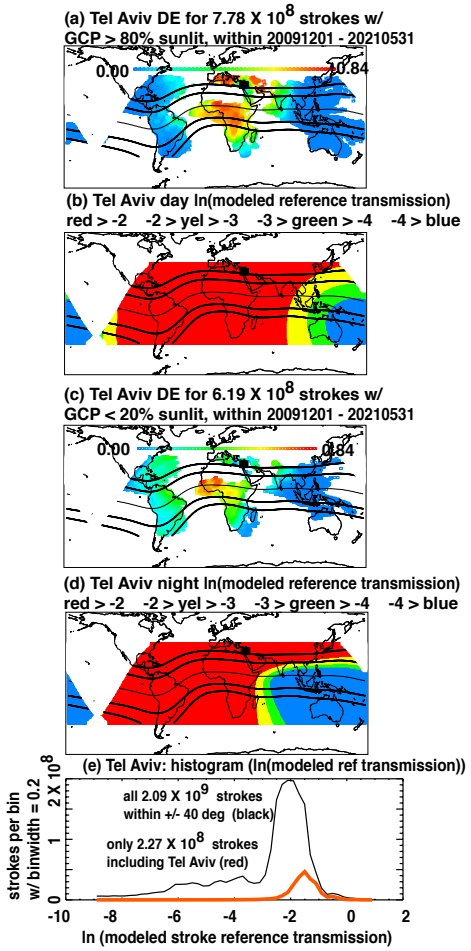

Figure A6: Similar to Figure 5, but for Tel Aviv station.

Acknowledgements

The authors are using data from the World Wide Lightning Location Network, a collaborative consortium of over seventy worldwide collaborators, managed at the University of Washington. The data would not exist but for the cooperative efforts of all of WWLLN's participants. For sale to researchers who are not WWLLN participants, WWLLN data are available, at a nominal price to cover overhead costs of running the network, and archiving / distributing the data. To find out about such data access, see http://wwlln.net/

References

Barber, N. F., and D. D. Crombie (1959), V. L. F. reflections from the ionosphere in the presence of a transverse magnetic field, *Journal of Atmospheric and Terrestrial Physics*, *16*, 37-45.

Bickel, J. E., J. A. Ferguson, and G. V. Stanley (1970), Experimental observation of magnetic field effects on VLF propagation at night, *Radio Sci.*, *5*(1), 19-25.

Budden, K. G. (1985), *The Propagation of Radio Waves*, 669 pp., Cambridge University Press, Cambridge.

Christian, H. J., et al. (2003), Global frequency and distribution of lightning as observed from space by the Optical Transient Detector, *J. Geophys. Res.*, *108*(D1), 4005, doi:10.1029/2002JD002347, doi:10.1029/2002JD002347.

Crombie, D. D. (1958), Differences between the east-west and west-east propagation of VLF signals over long distances, *Journal of Atmospheric and Terrestrial Physics*, *12*(2-3), 110-117.

Cummer, S. A. (2000), Modeling electromagnetic propagation in the Earth-ionosphere waveguide, *IEEE Trans. Antennas Propag.*, *48*(9), 1420-1429.

Hutchins, M. L. (2014), Source, propagation, and effects of lightning in the Earth-ionosphere system, PhD thesis, 156 pp, University of Washington.

Hutchins, M. L., R. H. Holtzworth, C. J. Rodger, and J. B. Brundell (2012), Far-field power of lightning strokes as measured by the World Wide Lightning Location Network, *J. Atmos. Oceanic Technol*, *29*, doi: 10.1175/JTECH-D-11-00174, 1102-1110, doi:10.1175/JTECH-D-11-00174.

Hutchins, M. L., A. R. Jacobson, R. H. Holzworth, and J. B. Brundell (2013), Azimuthal dependence of VLF propagation, *J. Geophys. Res.*, *118*, 1-5, doi:10.1002/jgra.50533, doi:10.1002/jgra.50533.

Jacobson, A. R., R. Holzworth, and X.-M. Shao (2010), Full-wave reflection of lightning long-wave radio pulses from the ionospheric D-region: Comparison with midday observations of broadband lightning signals, *J. Geophys. Res. -Space*, *115*, A00E27, doi:10.1029/2009JA014540, doi:10.1029/2009JA014540.

Jacobson, A. R., R. H. Holzworth, and J. B. Brundell (2021), Using the World Wide Lightning Location Network (WWLLN) to Study Very Low Frequency Transmission in the Earth-Ionosphere Waveguide: 1. Comparison with a Full-Wave Model, *Radio Science*, *56*, doi:10.1029/2021RS007293.

Jacobson, A. R., X. Shao, and R. H. Holzworth (2009), Full-wave reflection of lightning long-wave radio pulses from the ionospheric D-region: Numerical model, *J. Geophys. Res.- Space*, *114*, A03303, doi:10.1029/2008JA013642, doi:10.1029/2008JA013642.

Jacobson, A. R., X.-M. Shao, and E. Lay (2012), Time-domain waveform, and azimuth variation, of ionospherically reflected VLF/LF radio emissions from lightning, *Radio Sci.*, *47*, RS4001, doi:10.1029/2012RS004980.

Pappert, R. A., and J. A. Ferguson (1986), VLF/LF mode conversion model calculations for air to air transmissions in the Earth-ionosphere waveguide, *Radio Sci.*, *21*, 551-558.

Pappert, R. A., and L. R. Hitney (1988), Empirical modeling of nighttime easterly and westerly VLF propagation in the Earth-ionosphere waveguide, *Radio Sci.*, *23*(4), 599-611.

Piggott, W. R., M. L. V. Pitteway, and E. V. Thrane (1965), The numerical calculation of wave-fields, reflexion coefficients and polarizations for long radio waves in the lower ionosphere. II, *Phil. Trans. Roy. Soc. Lon.*, *257*(1079), 243-271.

Pitteway, M. L. V. (1965), The numerical calculation of wave-fields, reflexion coefficients and polarizations for long radio waves in the lower ionosphere. I, *Phil. Trans. Roy. Soc. Lon.*, *257*(1079), 219-241.

Taylor, W. L. (1960), VLF attenuation for East-West and West-East daytime propagation using atmospherics, *Journal of Geophysical Research*, *65*(7), 1933-1938.

V-MOD, I. W. G. (2010), International Geomagnetic Reference Field: the eleventh generation, *Geophys. J. International*, *183*(3), 1216-1230, doi:10.1111/j.1365-246X.2010.04804.x.

Volland, H. (Ed.) (1995), *Handbook of atmospheric electrodynamics*, CRC Press, Boca Raton, Florida, USA.

Wait, J. R., and K. Spies (1960), Influence of Earth curvature and the terrestrial magnetic field on VLF propagation, *Journal of Geophysical Research*, *65*(8), 2325-2331.

Wait, J. R., and K. P. Spies (1964), NBS Technical Note 300: Characteristics of the Earth-ionosphere waveguide for VLF radio waves, edited by U. S. D. o. C. National Bureau of Standards (now National Institute of Standards and Technology, NBS.

Yabroff, I. W. (1957), Reflection at a Sharply-Bounded Ionosphere, *Proc. Inst. Radio Engrs.*, *45*, 750-753.

Figure captions

Figure 1: Model amplitude reflectivity (vertical axis) vs propagation magnetic azimuth (horizontal axis). Color marks magnetic dip angle, from 5° (blue) to 85° (red). Curve for dip angle = 45° is dashed. Model assumes angle-of-incidence is 85°, and is averaged over the band 5 - 20 kHz. (a) Day case. (b) Night case, with labels on curves for dip angle = 30, 45°. The horizontal black line on both panels is through the minimum of the curve for dip angle = 45.° in (b). See Table 1 for parameter values.

Figure 2: Comparison of observed Atuona detection efficiency against strokes in two roughly equidistant, rectangular geographic boxes. (a) Showing the East box, over northwestern South America. (b) For all strokes in East box, showing the distribution of fraction of instantaneous path (to Atuona) that is daylit. This includes all strokes in the East box, not just those detected by Atuona. Horizontal resolution is 0.01. (c) Detection efficiency (DE) of Atuona against strokes in East box, as a function of the instantaneous daylit fraction of the path. (d) Showing the West box. (e) For all strokes in West box, showing the distribution of fraction of instantaneous path (to Atuona) that is daylit. (f) Detection efficiency (DE) of Atuona against strokes in West box, as a function of the instantaneous daylit fraction of the path. Note the order-of-magnitude difference in DE scales between (c) East and (f) West boxes.

Figure 3: Geomagnetic setting of each of the ten selected stations. Each station is shown as a rectangle, either white or black so as to contrast with the background. The color shading of the background is magnitude of dip angle, from 0 (black) to 74° (red). Only (i) has a different color

scale: 0 (black) to 76° (red). The colors are shown within latitude bands -40 to +40°, except -30 to +50° for (i) Honolulu. Also, discrete curves are drawn, where dip angle = -30, -45, +30, and +45°. The white cone at each station's antipode is excluded from the analyses, because the Great Circle Paths from strokes within those cones extend poleward of +/- 55° latitude.

Figure 4: Patterns of detection/non-detection for Atuona. (a) Spatial density of WWLLN-located strokes within the latitude band for which the Great Circle Path is > 80% sunlit. The maximum for this density is red, while blue is 1% of the maximum. White areas outside of the antipodal cone correspond to stroke density less than 1% of the maximum. The discrete lines are at dip angle = 0, +/- 30, and +/- 45°. Neither the stroke density, nor the curves, are shown within the antipodal cone or outside of the latitude band. (b) Spatial density of the subset of strokes in whose location Atuona participates, for which the Great Circle Path is > 80% sunlit. The new maximum is shown as red, and 1% of this new maximum is shown as blue. (c) Similar to (a) but for Great Circle Paths < 20% sunlit. (d) Similar to (b) but for Great Circle Paths < 20% sunlit.

Figure 5: Observed and predicted results on Atuona detection efficiency. (a) Map of observed detection efficiency by the Atuona station for the strokes each of whose paths to Atuona are >80% sunlit. Color scale runs from 0.00 (blue) to 0.82 (red). Pixel resolution is 1° X 1°. White areas outside of the antipodal cone correspond to stroke density less than 1% of the maximum. The discrete lines are at dip angle = 0, +/- 30, and +/- 45°. (b) Predicted logarithmic reference transmission for the contrived pure-day case. The pixels are whitened in the antipodal cone and outside of the latitude band. The transmission values are shown as ranges from the highest transmission, > -2 (red), through less high, -2 to -3 (yellow), to even lower, -3 to -4 (green), to

lowest transmission, < -4 (blue). (c) Similar to (a), but for the paths <20% sunlit. The color scale is the same as used in (a). (d) Similar to (b), but for the contrived pure-night case. (e) Distribution of the modeled logarithmic reference transmission, using exact instantaneous local solar zenith angle at each segment of each path from the stroke to the Atuona station. Black curve: All strokes within the latitude band. Red curve: Only those strokes in whose location Atuona participates.

Figure 6: Similar to Figure 5, but for Peru station.

Figure 7: Similar to Figure 5, but for Singapore station.

Figure 8: Similar to Figure 5, but for Honolulu station.

Figure A1: Similar to Figure 5, but for Tahiti station.

Figure A2: Similar to Figure 5, but for the Costa Rica station.

Figure A3: Similar to Figure 5, but for the Belem station.

Figure A4: Similar to Figure 5, but for the Dakar station.

Figure A5: Similar to Figure 5, but for the Pune station.

Figure A6: Similar to Figure 5, but for the Tel Aviv station.

parameter	day model	night model
reference electron density n_{e0}	$3X10^8$ m^{-3}	$3X10^8$ m^{-3}
density reference height z_0	73 km	85 km
density logarithmic derivative q	0.30 km^{-1}	0.45 km^{-1}
reference collision rate ν_0	$5X10^6$ s^{-1}	$5X10^6$ s^{-1}
collision-rate reference height h_0	70 km	70 km
collision-rate logarithmic derivative p	0.15 km^{-1}	0.15 km^{-1}

Table 1: Parameters for exponential D-layer model of electron density $n_e(z) = n_{e0} exp(q(z - z_0))$ and electron-neutral collision rate $\nu_{en}=\nu_0$ exp(-p(z-h_0))

Station lon E, lat N (deg)	file range (yyyymmdd)	# files used	lat range (deg N)	# of strokes in lat range	# including this station	
Atuona -139.0, -9.8	20151030 to 20210531	1658	-40 to 40	$9.21 X 10^8$	$1.09 X 10^8$	
Tahiti -149.6, -17.6	20091201 to 20210531	3687	-40 to 40	$1.94 X 10^9$	$1.93 X 10^8$	
Peru -75.3, -12.0	20091201 to 20210506	3633	-40 to 40	$1.89 X 10^9$	$2.38 X 10^8$	
Costa Rica -84.0, 9.9	20091201 to 20210531	3835	-40 to 40	$2.01 X 10^9$	$2.92 X 10^8$	
Belem -48.4, -1.5	20190705 to 20210531	566	-40 to 40	$3.21 X 10^8$	$4.58 X 10^7$	
Dakar -17.5, 14.7	20100909 to 20210401	2168	-40 to 40	$1.16 X 10^9$	$1.50 X 10^8$	
Pune 73.8, 18.5	20130522 to 20210522	1610	-40 to 40	$9.20 X 10^8$	$6.98 X 10^7$	
Singapore 103.8, 1.3	20091201 to 20210531	3553	-40 to 40	$1.86 X 10^9$	$1.37 X 10^8$	
Honolulu -157.8, 21.3	20091201 to 20210531	3873	-30 to 50	$2.05 X 10^9$	$2.74 X 10^8$	
Tel Aviv 34.8, 32.1	20091201 to 20210531	3987	-40 to 40	$2.05 X 10^9$	$2.27 X 10^8$	

Table 2: Data from the ten stations used in this study